High Power Laser Science and Engineering, (2025), Vol. 13, e55, 12 pages.
doi:10.1017/hpl.2025.26

HIGH POWER LASER SCIENCE AND ENGINEERING

RESEARCH ARTICLE

Compact laser amplifier with high gain based on Nd^{3+}-doped SrF_2 crystal

Siqi Long[1], Lailin Ji[1], Xianghe Guan[1], Yong Cui[1], Fujian Li[1], Zhonghan Zhang[2], Tianxiong Zhang[1], Zhen Zhang[2], Jian Shi[1], Dong Liu[1], Ruijing He[1], Xiaohui Zhao[1], Tao Wang[1], Xiaoli Li[1], Jianjun Cao[3], Jinsheng Liu[1], Yanqi Gao[1], Liangbi Su[2], and Zhan Sui[1]

[1] *Shanghai Institute of Laser Plasma, China Academy of Engineering Physics, Shanghai, China*

[2] *State Key Laboratory of Functional Crystals and Devices, Shanghai Institute of Ceramics, Chinese Academy of Sciences, Shanghai, China*

[3] *School of Science, Jiangnan University, Wuxi, China*

(Received 27 September 2024; revised 17 January 2025; accepted 4 March 2025)

Abstract

High gain greater than 10^6 is crucial for the preamplifiers of joule-class high-energy lasers. In this work, we present a specially designed compact amplifier using 0.5%Nd,5%Gd:SrF_2 and 0.5%Nd,5%Y:SrF_2 crystals. The irregular crystal shape enhances the gain length of the laser beam and helps suppress parasitic oscillations. The amplified spontaneous emission (ASE) induced by the high gain is analyzed through ray tracing. The balance between gain and ASE is estimated via numerical simulation. The gain spectral characteristics of the two-stage two-pass amplifier are examined, demonstrating the advantages of using different crystals, with bandwidths up to 8 nm and gains over 10^6. In addition, the temperature and stress distributions in the Nd,Gd:SrF_2 crystal are simulated. This work is expected to contribute to the development of high-peak-power (≥terawatt-class) high-energy (joule-class) laser devices.

Keywords: amplified spontaneous emission; broadband output; fluoride laser crystal; high gain; laser amplifier

1. Introduction

High-peak-power (≥terawatt-class), high-energy (joule-class) pulsed lasers have garnered significant attention due to their applications in inertial confinement fusion, high-energy-density physics, laboratory astrophysics and laser plasma-wakefield acceleration[1–6]. Most preamplifiers for these lasers utilize regenerative amplifiers with high gain ($>10^6$), high repetition rate and excellent beam quality. A pulse picker is then employed to reduce the repetition rate. However, the regenerative amplifiers require highly stable resonators. These resonators are typically over a meter long and contain active components, making regenerative amplifiers relatively complex and bulky[7,8]. Alternatively, multipass amplifiers, which allow the beam to pass through the gain medium multiple times without the need for a resonant cavity, are commonly used for high-energy amplification. However, most multipass amplifiers require precise imaging optics to achieve both high gain and excellent beam quality[9,10]. Therefore, for high-peak-power, high-energy lasers, it is important to design a simple preamplifier that combines miniaturization with high gain.

The typical gain materials used in high-peak-power, high-energy laser systems are Ti:sapphire crystal and Nd:glass. Parasitic lasing and amplified spontaneous emission (ASE) in Ti:sapphire remain challenging issues[11,12]. The thermal conductivity of Nd:glass is relatively low (~0.56 W/(m·K)), which limits the ability to increase the repetition rate of the laser system[13]. Neodymium-doped strontium fluoride (SrF_2) crystals have attracted much attention as a laser gain medium due to their low nonlinear refractive index, broad transparency, wide emission bandwidth and relatively high thermal conductivity[14,15]. Furthermore, Gd^{3+} and Y^{3+} as buffer ions can mitigate aggregation-induced fluorescence quenching of Nd^{3+} ions, thereby increasing the quantum yield[16,17]. The feasibility of using Nd,Gd:SrF_2 and Nd,Y:SrF_2 in resonators has been demonstrated. For example, the output power and slope efficiency of continuous-wave lasers based on the Nd,Gd:SrF_2 crystal can reach 992 mW and 42.7%, respectively[18,19], while the pulse

Correspondence to: L. Ji and Z. Sui, Shanghai Institute of Laser Plasma, China Academy of Engineering Physics, Shanghai 201800, China. Emails: jsycjll@siom.ac.cn (L. Ji); lqling@vip.163.com (Z. Sui)

duration in mode-locked operation can be as short as 321 fs[20]. Using Nd,Y:SrF_2 as the gain medium, the output power and slope efficiency of continuous-wave lasers are 750 mW and 69%, respectively, and the pulse durations in *Q*-switched and mode-locked operating modes range from 169 ns to 97 fs[21–23]. The application of Nd,Y:SrF_2 crystals in regenerative amplifiers has also been reported[24,25]. However, the simultaneous use of Nd,Gd:SrF_2 and Nd,Y:SrF_2 in high-gain multipass amplifiers, offering the advantages of miniaturization and high flexibility, has not yet been explored.

In this paper, a compact two-stage two-pass laser amplifier based on Nd,Gd:SrF_2 and Nd,Y:SrF_2 is studied. The irregular crystal shape is selected to arrange complex beam amplification paths and suppress parasitic oscillations. The ASE, broadband characteristics, temperature and stress distributions of the amplifier are analyzed. To the best of our knowledge, this is the first proposal for a compact multipass amplifier with a gain exceeding 10^6, utilizing different SrF_2 crystals.

2. Design of the compact laser amplifier

2.1. Spectral properties of the SrF_2 crystal

The 0.5%Nd,5%Gd:SrF_2 and 0.5%Nd,5%Y:SrF_2 disordered crystals used in this study can be grown using the vertical Bridgman method[26]. Their absorption and emission spectra are shown in Figure 1. The strongest absorption peak for both 0.5%Nd,5%Gd:SrF_2 and 0.5%Nd,5%Y:SrF_2 occurs around 797 nm, which is well-suited for commercial laser diode (LD) pumping. The two emission peaks for 0.5%Nd,5%Gd:SrF_2 are at 1052 and 1059 nm, while the two emission peaks for 0.5%Nd,5%Y:SrF_2 are at 1050 and 1057 nm. When the two crystals are used together, the emission spectrum is approximately flat at the top, which helps to mitigate the gain narrowing effect during amplification[27–29]. The key parameters of the crystals are summarized in Table 1.

2.2. Configuration of the amplifier

There are two methods to achieve high gain in an amplifier: one is to increase the small signal gain coefficient, and the other is to increase the optical path length. The former is influenced by the crystal's intrinsic parameters and the pump energy density, while the latter is determined by the crystal geometry and the beam trajectory. In the pursuit of miniaturization, the design of the crystal shape becomes particularly important.

The proposed compact amplifier configuration is shown in Figure 2(a), where two identical isosceles right-angled triangular prisms are cut on a cuboid crystal, and the two cross-sections of the prisms serve as the incident and exit planes, respectively. This shape can also be considered a combination of a cuboid and a quadrangular prism. The bottom surface of the cuboid is square, while the bottom surface of the quadrangular prism is an isosceles trapezoid. The lower base of the trapezoid and the side of the square have the same length, with the height of the trapezoid being one-fourth of the side length of the square. Three LDs are placed on three sides of the crystal for pumping. The refractive index of the SrF_2 crystal is about 1.4328@1.05 μm[30], so the angle for total-internal reflection (TIR) is 44.2615°. The beam undergoes normal incidence and is reflected seven times within the designed amplifier due to TIR.

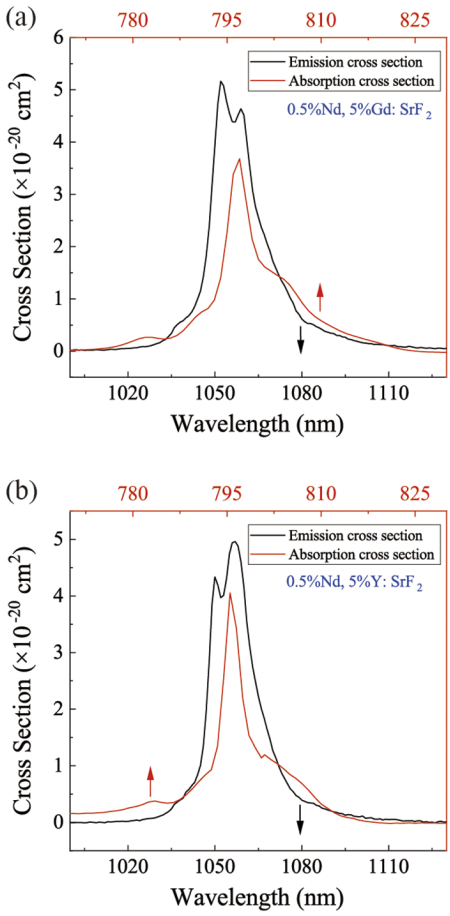

Figure 1. Emission and absorption spectra for (a) 0.5%Nd,5%Gd:SrF_2 crystal and (b) 0.5%Nd,5%Y:SrF_2 crystal.

Table 1. The parameters of 0.5%Nd,5%Gd:SrF_2 and 0.5%Nd,5%Y:SrF_2.

Sample	Peak absorption cross-section ($\times 10^{-20}$ cm^2)	Peak emission cross-section ($\times 10^{-20}$ cm^2)	Emission linewidth (nm)	Fluorescence lifetime (μs)
Nd,Gd:SrF_2	3.68@797 nm	5.16@1052 nm	17	343
Nd,Y:SrF_2	4.06@796 nm	4.96@1057 nm	16	356

https://doi.org/10.1017/hpl.2025.26 Published online by Cambridge University Press

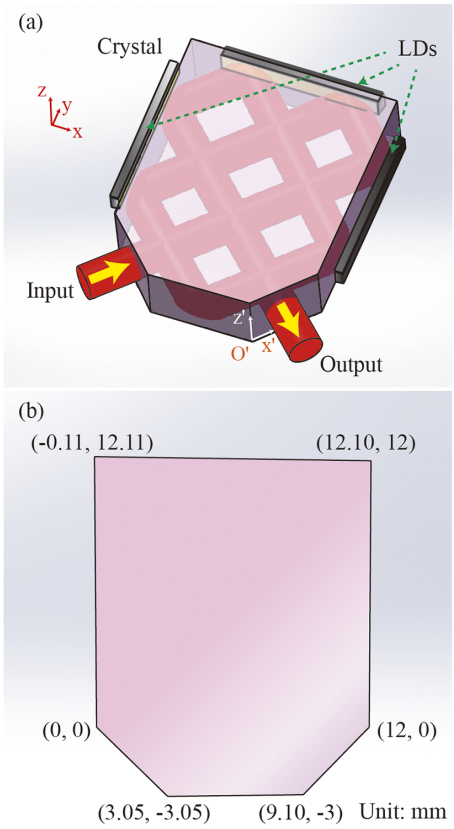

Figure 2. (a) Configuration of the compact amplifier. (b) Coordinates of the crystal.

Multiple parallel surfaces can easily lead to parasitic oscillations, which significantly affect the gain performance[31]. To mitigate this issue, the bottom and top surfaces of each crystal are roughened, and in the *x*–*y* plane, most sides are tilted by 0.5° or 1° from the original position. Figure 2(b) shows the coordinates of the crystal in the *x*–*y* plane. The side length of the square is about 12 mm, which is compatible with the bar size of commercial LDs.

2.3. Setup of the two-stage two-pass amplifier

To increase the gain of the laser amplification system, we designed a two-stage, two-pass amplifier, as shown in Figure 3. Firstly, the seed pulse is p-polarized by passing through a thin-film polarizer (TFP) and injected into amplifier 1 and amplifier 2. Secondly, the beam is directed to a quarter-wave plate (QWP) and then to the end-mirror, which rotates the polarization by 90° after two passes. Thirdly, the returned s-polarized pulse passes through amplifier 2 and amplifier 1 again. Finally, the amplified beam is reflected by the TFP and exits the system. It should be noted that thermally induced depolarization, caused by temperature gradients, could disrupt the operation of the amplifier. Therefore, it is recommended to use the 'zero depolarization' orientation of the crystals, which helps minimize the energy loss[32].

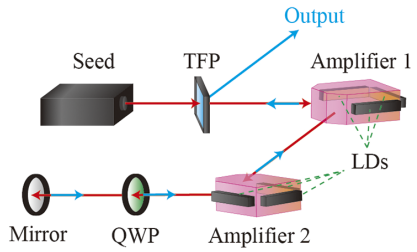

Figure 3. Schematic of the two-stage two-pass amplifier.

3. Amplified spontaneous emission of a single amplifier

The total gain target of the two-stage two-pass amplifier is greater than 10^6, which is accompanied by strong ASE. Ray tracing is used to analyze the ASE due to the irregular geometry of the crystal[33]. Since the properties of 0.5%Nd,5%Gd:SrF_2 and 0.5%Nd,5%Y:SrF_2 are similar, we take the former as an example for this analysis.

3.1. Calculation model of ASE

In the simulation, the crystal is divided into N parts, where each part is treated as an energy point with the same volume, except for the two angles. The energy supplied to the crystal by the LDs can be expressed as follows[34]:

$$E = Pt_{\mathrm{p}}\eta_{\mathrm{T}}\eta_{\mathrm{A}}, \tag{1}$$

where P is the pump power, t_{p} is the pump time and η_{T} is the pump transmission efficiency. η_{A} is the absorption efficiency, with its calculation model varying based on the object of calculation. When the small signal gain coefficient is calculated, η_{A} refers to the total absorption efficiency of the crystal. When the energy distribution is calculated, η_{A} is the absorption efficiency of a part of crystal. The expression of η_{A} is as follows:

$$\eta_{\mathrm{A}} = \begin{cases} 1-\exp(-\alpha_{\mathrm{D}} l) & (\text{calculate } g_0) \\ \exp(-\alpha_{\mathrm{D}} l_2) - \exp(-\alpha_{\mathrm{D}} l_1) & (\text{calculate the energy distribution}) \end{cases}, \tag{2}$$

where α_{D} is the absorption coefficient of the crystal, which is 3.45 cm^{-1}, l is the total length of the LD beam passing through the crystal, and l_1 and l_2 represent the farthest and nearest propagation distances, respectively, that the LD beam travels to reach the boundary of the calculated part of the crystal. The pump time is divided into t' parts, and the increased energy in time interval (Δt) is E/t'. In two adjacent time intervals, the earlier one is defined as the 'previous time', and the later one as the 'current time'. The stored energy at the previous time (E') consists of two parts: the energy supplied to the crystal by the LDs and the energy consumed by the ASE effect (the calculation model for ASE is described later). The stored energy at the current time is as follows:

$$E_{\mathrm{S}} = \left(E' + \frac{E}{t'}\right)\eta_{\mathrm{S}} \exp\left(-\frac{\Delta t}{\tau_{\mathrm{f}}}\right), \tag{3}$$

https://doi.org/10.1017/hpl.2025.26 Published online by Cambridge University Press

Table 2. Values of the parameters in the ASE simulation.

Parameter	N	t_p	t'	η_T	η_S	η_A (for g_0)	V	N_{ray}
Value	870	320 μs	10	0.9900	0.7576	0.9840	0.4098 cm^3	21,025

where η_S is the Stokes efficiency and τ_f is the fluorescence lifetime. The small signal gain coefficient in Δt is as follows:

$$g_0 = \frac{E_S \sigma}{Vh\nu}, \tag{4}$$

where σ is the peak emission cross-section, V is the pump volume, h is Planck's constant and ν is the light frequency. The energy produced by spontaneous emission (SE) is as follows:

$$E_{SE} = \left(E' + \frac{E}{t'}\right)\eta_S\left[1 - \exp\left(-\frac{\Delta t}{\tau_f}\right)\right]. \tag{5}$$

Since the generation of SE is random, it is assumed that the probability of generating SE rays at different angles in 4π space is uniform. The number of rays per part is denoted as N_{ray}. The total SE energy of each part is denoted as E'_{SE}, so the initial energy of a ray (E_{ray}) is equal to E'_{SE}/N_{ray}. The parameters used in the ASE simulation are listed in Tables 1 and 2.

Figure 4 shows the flow chart of the ASE calculation model. The first step is to select the time slice. In the second step, energy distribution in the crystal is calculated using Equations (1)–(5). The third step involves selecting the starting point and the direction of the trace. The coordinates (x, y, z) in millimeters represent the position of the point. To save computational time, only one z-value is considered, which is half the height of the crystal, since the crystal has the same shape in the z-direction. The direction in 4π space is given by two angles: the angle between the ray and the z-axis (θ), and the angle between the projection of the ray in the x–y plane and the x-axis (φ). The fourth step involves comparing the ray energy with the energy threshold. The energy threshold serves as the cutoff condition for ray tracing. If the threshold is set too high, the simulation accuracy decreases. Conversely, if the threshold is set too low, the simulation time increases. After comprehensive consideration, the threshold is set to 5% of the initial ray energy. When the ray energy is lower than the threshold, the simulation returns to the third step to select another point. Otherwise it proceeds to the next step. The fifth step involves ray tracing. The amplified ray energy can be expressed as follows:

$$E_A = E_{ray}\exp\left[(g_0 - \alpha)L\right]R, \tag{6}$$

where α is the loss coefficient of the crystal (0.0015 cm^{-1}) and L is the optical path length. The reflections (R) on the two rough surfaces of the crystal are neglected, while the reflection coefficients of the remaining surfaces are calculated using the Fresnel equations. The sixth step is to record the position and energy of the ray, and then return to the fourth step. After the energy of all rays has been calculated, the simulation returns to the first step to select the next time slice. The model continues until the energy for all time slices has been calculated.

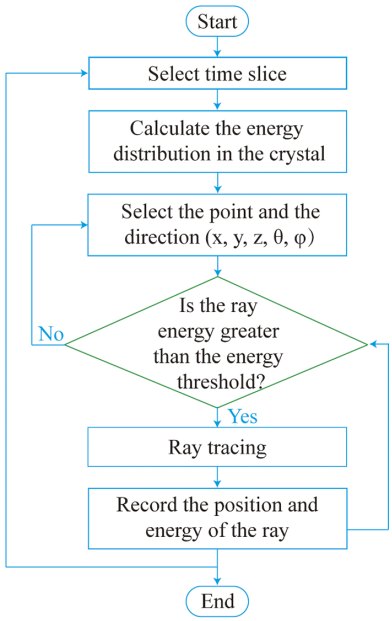

Figure 4. Flow chart of the ASE calculation model.

3.2. *Calculation results of ASE*

To simplify the calculation, the divergence angle of the LD is set to zero. This assumption can be fulfilled using collimation lens arrays, which can control the fast and slow axis divergence angles of LD bars to within 0.35°[35–37]. The energy distribution is shown in Figure 5(a) with normalized values. In the x–y plane, more energy is concentrated at the two upper corners of the crystal, while the energy is almost zero at the bottom of the crystal. The relation between the small signal gain coefficient g_0 and pump time is plotted in Figure 5(b). The dashed lines indicate the results when ASE is not considered, and the solid lines indicate the results when ASE is included. The value of g_0 gradually increases, with the growth rate slowing down as the simulation time progresses. In addition, the influence of ASE on g_0 increases with higher pump power. For example, when the pump time is set to 320 μs, the presence of ASE reduces g_0 by 0.0764 cm^{-1} when the pump power is 3.6 kW, and by 0.1602 cm^{-1} when the pump power is 7.2 kW. Figures 5(c) and 5(d) show the ASE energy distribution of the output surface $x'O'z'$ when the pump power is 6 kW. The ASE energy

https://doi.org/10.1017/hpl.2025.26 Published online by Cambridge University Press

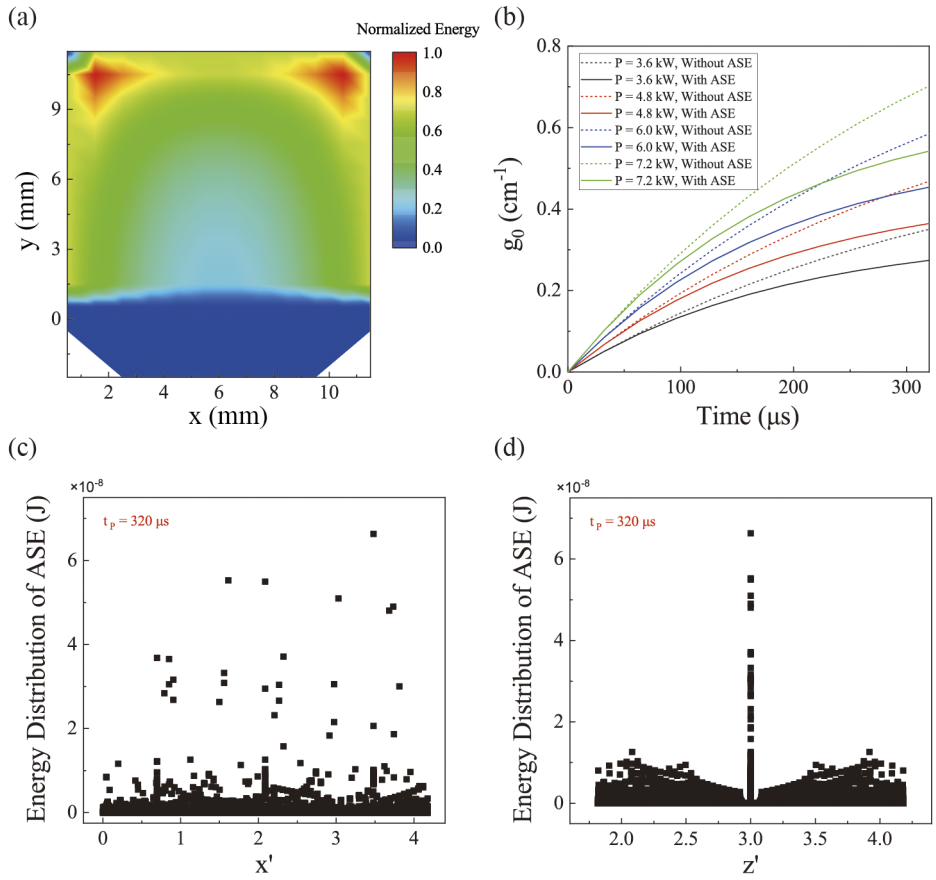

Figure 5. (a) The normalized energy distribution. (b) The relation between the small signal gain coefficient and the pump time. (c) The energy distribution of ASE along the x'-axis. (d) The energy distribution of ASE along the z'-axis.

increases slightly along the x'-axis due to the asymmetrical shape in the x–y plane. In the z'-direction, the ASE energy is the highest in the middle, with a symmetrical distribution on both sides. This is because only the beam from the starting points in the middle of the crystal ($z = 3$ mm) is tracked. The ray is reflected most of the time within the crystal, and the gain is highest when $\theta = 0°$. The ray path to both ends of the z'-axis is longer, so the gain is also relatively higher when $\theta \neq 0°$. In summary, the higher the pump energy, the higher the gain, and the stronger the ASE effect. Therefore, to achieve the desired g_0, the pump energy must be increased beyond the value required to reach the target g_0 without considering ASE.

4. Broadband pulse propagation of the two-stage two-pass amplifier

The presence of anti-reflection coatings, the processing errors of the crystal and LDs and the insertion of other optical elements can influence the ASE discussed in Section 3. To simplify the calculation, the effect of ASE on the broadband pulse propagation is not considered in this analysis. However, the pump parameters, accounting for the influence of ASE, are provided at the end of this section. Since the designed amplifier is operated in a single-shot mode, the thermal effects are not taken into account.

4.1. Calculation model of broadband pulse propagation

The broadband characteristics are simulated using MATLAB software. The broadband pulse propagation in the amplifier is derived from the resonant-dipole equation, the population inversion equation and Maxwell's equation. During the derivation process, several methodologies, including Fourier transformation and inverse transformation, the slowly varying envelope approximation and the fourth-order Runge–Kutta method, are employed. The resulting expression is given as follows[38]:

$$\begin{aligned}
&\frac{\partial E_0(z,t)}{\partial z} = -i\frac{\omega_0}{2\varepsilon c}P_0(z,t) + i\frac{\beta''}{2}\frac{\partial^2 E_0(z,t)}{\partial t^2} - i\frac{\beta_2}{2}|E_0(z,t)|^2 E_0(z,t),\\
&\frac{\partial P_0(z,t)}{\partial t} + \frac{\Delta\omega_a}{2}\left[1 + i\frac{2(\omega_0-\omega_a)}{\Delta\omega_a}\right]P_0(z,t) = i\frac{K}{2\omega_0}N(z,t)E_0(z,t),\\
&\frac{\partial N(z,t)}{\partial t} = i\frac{2^*}{4\hbar}\left[E_0^*(z,t)P_0(z,t) - E_0(z,t)P_0^*(z,t)\right],
\end{aligned} \tag{7}$$

https://doi.org/10.1017/hpl.2025.26 Published online by Cambridge University Press

where $E_0(z,t)$ is the electric field intensity, ω_0 is the carrier frequency, ε is the dielectric constant of the amplifier, c is the velocity of light in the amplifier, $P_0(z,t)$ is the resonant polarization, β'' is the second-order derivative of the propagation constant at ω_0, the constant β_2 is equal to $2\pi n_{2E}/\lambda_0$, n_{2E} is the nonlinear refractive index, which is 1.4628×10^{-20} m^2/W[39], λ_0 is the laser wavelength in vacuum, $\Delta\omega_a$ is the full atomic linewidth, ω_a is the center frequency of the line, the constant K is equal to $\varepsilon c\sigma\Delta\omega_a$, $N(z,t)$ is the population inversion, 2^* is a dimensionless population saturation factor with values between 1 and 2 and $\hbar$ is equal to $h/(2\pi)$. The seed pulse waveform is defined as a fourth-order ultra-Gaussian distribution. It has a beam diameter of 2 mm, a wavelength of 1053 nm, a pulse duration of 3.5 ns, an energy of 3 nJ and a bandwidth of 18 nm. The beam passes through the two-stage two-pass amplifier, as depicted in Figure 3, where the pump power is 6 kW. The reflectance of the TFP for the s-polarized pulse and the reflectance of the mirror are both 99%. Meanwhile, the transmittance of the TFP for the p-polarized pulse and the transmittance of other optical elements reach 99%. The thicknesses of the TFP and QWP are 3 and 1.6 mm, respectively.

4.2. Calculation results of broadband pulse propagation

The two-stage two-pass amplifier features three configurations based on the type of crystal utilized: (1) both crystals are 0.5%Nd,5%Gd:SrF_2; (2) both crystals are 0.5%Nd,5%Y:SrF_2; and (3) the first crystal is 0.5%Nd,5%Gd:SrF_2 while the second one is 0.5%Nd,5%Y:SrF_2. When both crystals are of the same type, the pump time is set to be equal and is incremented by 5 μs at a time until the output energy exceeds 4.8 mJ. In cases where the crystal types differ, the increment step for the pump time of Nd,Gd:SrF_2 is 20 μs, and the pump time for Nd,Y:SrF_2 is increased by 5 μs at a time until the output energy exceeds 4.8 mJ.

The normalized distributions of the output pulse are shown in Figures 6(a)–6(d) when the crystal type is the same. The black, red and blue lines represent the distribution of the input pulse, the pulse after the first amplification and the output pulse, respectively. 'ΔTime' and 'ΔWavelength' are the offset time and wavelength relative to the reference time and wavelength, respectively. During the amplification process, the width of both the time waveform and the spectrum narrows, and the normalized intensity difference between the main peak and the secondary peak increases. This narrowing of the output spectrum bandwidth leads to a large Fourier transform limited pulse duration, making it more challenging to achieve high peak power. To increase the output bandwidth, Nd,Gd:SrF_2 and Nd,Y:SrF_2 are used in combination. Figures 6(e) and 6(f) represent the time waveform distribution and the spectrum distribution of the output pulse, respectively. The broadband characteristics under diverse conditions are presented in Table 3. As the pump time of the first crystal increases and the pump time of the second crystal decreases, the normalized intensity of the secondary peak gradually approaches or even exceeds that of the main peak. Moreover, the bandwidth is more than doubled compared to using the same crystal type. This phenomenon highlights the advantage of simultaneously using crystals with different emission wavelengths. Furthermore, different emission wavelengths of crystals can be achieved by tuning the doping concentrations or co-dopant species, a strategy that can be applied not only to SrF_2 crystals but also to other substrate materials, such as calcium fluoride[40].

The additional phase acquired by the nonlinear effect during laser transmission is defined as the B-integral, and the expression is given by the following[41]:

$$B = \frac{2\pi n_{2E}}{\lambda_0}\int E_0(z,t)^2 \mathrm{d}z. \tag{8}$$

The B-integral of the two-stage two-pass amplifier is significantly lower than 1, which ensures the output pulse quality.

When the ASE is not considered, the pump power is 6 kW, the pump time for Nd,Gd:SrF_2 is 320 μs and the small signal gain coefficient of Nd,Gd:SrF_2 is 0.615 cm^{-1}. As shown in Figure 5(b), when the ASE is considered, the expression for the green solid line, which represents a pump power of 7.2 kW, is approximated by the following:

$$g_{0\,(7.2\mathrm{kW})} = 0.66504 - 0.66616\exp\left(-\frac{t_P}{188.49189}\right). \tag{9}$$

When $g_{0\,(7.2\mathrm{kW})}$ is 0.615, the corresponding pump time is 488 μs. The pump power of a commercial LD bar operating at a pump time of less than 500 μs and a repetition rate of less than 1 Hz can reach 500 W at 797 nm, and five bars can be placed within 2 mm. This design configuration is therefore feasible and should be realizable based on the given parameters.

5. Temperature and stress distributions of Nd,Gd:SrF_2 crystal

In Section 4, thermal effects were neglected as the amplifier operated in single-shot mode. This section investigates the temperature and stress distributions within the Nd,Gd:SrF_2 crystal, and illustrates its potential application in pulsed lasers for repetition rate operation.

5.1. Calculation model of temperature distribution

The temperature distribution of Nd,Gd:SrF_2 is simulated using COMSOL Multiphysics software. The transient-state equation to describe heat transfer in solids is given by the following[42]:

https://doi.org/10.1017/hpl.2025.26 Published online by Cambridge University Press

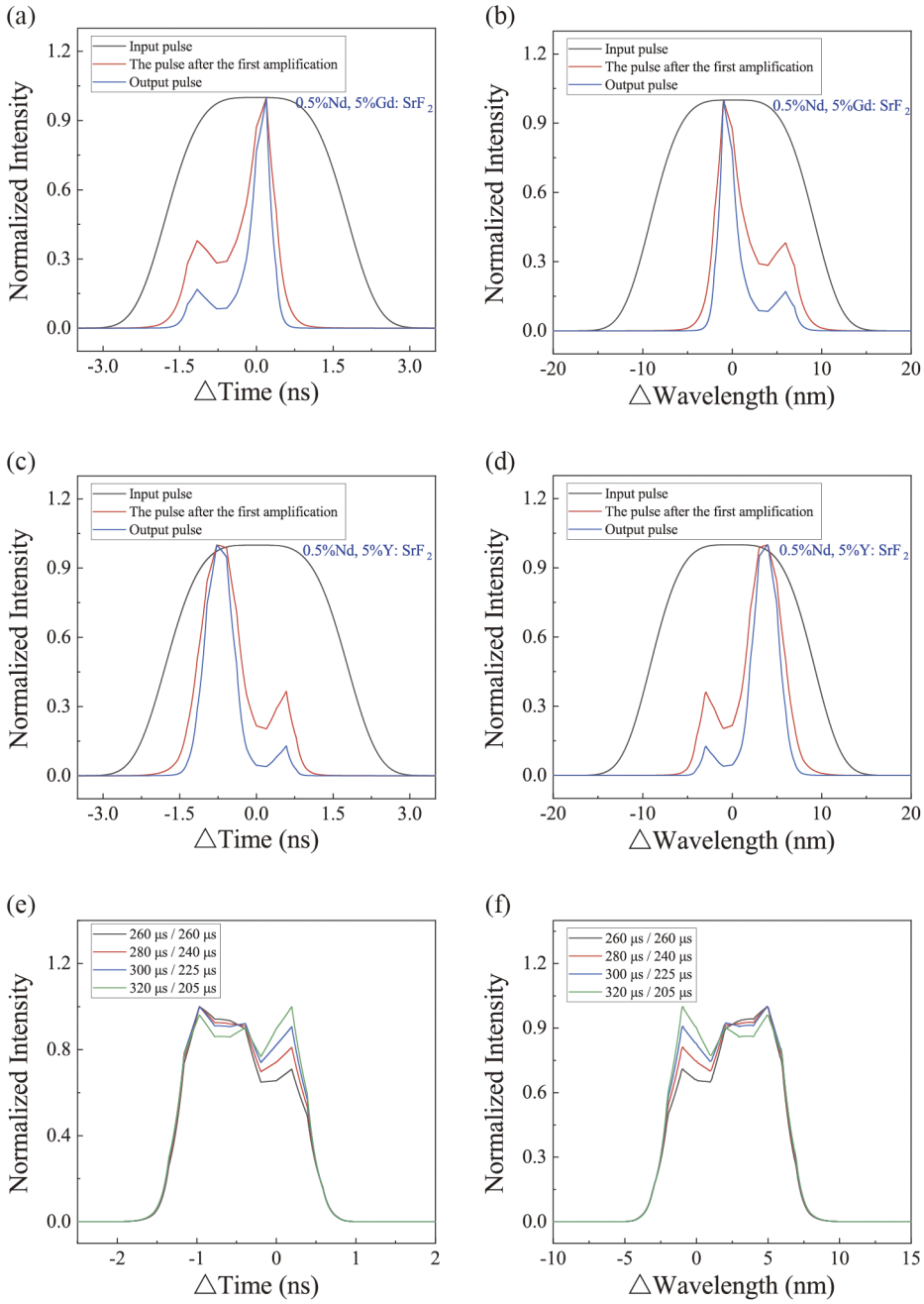

Figure 6. Normalized distributions of the output pulse under three configurations: (a), (b) both crystals are 0.5%Nd,5%Gd:SrF_2; (c), (d) both crystals are 0.5%Nd,5%Y:SrF_2; and (e), (f) the first crystal is 0.5%Nd,5%Gd:SrF_2 while the second crystal is 0.5%Nd,5%Y:SrF_2. (a), (c) and (e) are time waveforms, while (b), (d) and (f) are spectra.

Table 3. The broadband characteristic under various conditions.

Crystal 1	Pump time 1 (μs)	Crystal 2	Pump time 2 (μs)	Peak wavelength (nm)	Output bandwidth (nm)	Output energy (mJ)	B-integral ($\times 10^{-5}$)
Nd,Gd:SrF_2	240	Nd,Gd:SrF_2	240	1052.06	1.98	5.39	3.81
Nd,Y:SrF_2	265	Nd,Y:SrF_2	265	1056.93	3.36	5.76	3.12
Nd,Gd:SrF_2	260	Nd,Y:SrF_2	260	1057.92	8.30	5.05	1.50
Nd,Gd:SrF_2	280	Nd,Y:SrF_2	240	1057.94	8.44	5.03	1.37
Nd,Gd:SrF_2	300	Nd,Y:SrF_2	225	1057.94	8.53	5.33	1.35
Nd,Gd:SrF_2	320	Nd,Y:SrF_2	205	1052.05	8.56	4.91	1.14

https://doi.org/10.1017/hpl.2025.26 Published online by Cambridge University Press

$$\rho C_{\mathrm{p}} \frac{\partial T}{\partial t} + \nabla \cdot (-k \nabla T) = Q, \tag{10}$$

where ρ is the solid density, C_{p} is the solid heat capacity at constant pressure, T is the temperature, t is the simulation time and k is the thermal conductivity. Here, Q is the heat source, which can be written as follows:

$$Q_{(y\approx 12\ \mathrm{mm})} = \begin{cases} \frac{\alpha_{\mathrm{D}}(1-\eta_{\mathrm{S}})P_{\mathrm{s}}}{S_{\mathrm{LD}}} \exp\left[-\alpha_{\mathrm{D}}(l-y)\right] & (2\ \mathrm{mm} \le z \le 4\ \mathrm{mm}, 1\ \mathrm{mm} \le x \le 11\ \mathrm{mm}) \\ 0 & (\mathrm{else}) \end{cases}, \tag{11}$$

$$Q_{(x\approx 0\ \mathrm{mm})} = \begin{cases} \frac{\alpha_{\mathrm{D}}(1-\eta_{\mathrm{S}})P_{\mathrm{s}}}{S_{\mathrm{LD}}} \exp(-\alpha_{\mathrm{D}} x) & (2\ \mathrm{mm} \le z \le 4\ \mathrm{mm}, 1\ \mathrm{mm} \le y \le 11\ \mathrm{mm}) \\ 0 & (\mathrm{else}) \end{cases}, \tag{12}$$

$$Q_{(x\approx 12\ \mathrm{mm})} = \begin{cases} \frac{\alpha_{\mathrm{D}}(1-\eta_{\mathrm{S}})P_{\mathrm{s}}}{S_{\mathrm{LD}}} \exp[-\alpha_{\mathrm{D}}(l-x)] & (2\ \mathrm{mm} \le z \le 4\ \mathrm{mm}, 1\ \mathrm{mm} \le y \le 11\ \mathrm{mm}) \\ 0 & (\mathrm{else}) \end{cases}. \tag{13}$$

Here, S_{LD} is the area of the pump light and P_{s} is the pump power of a single LD, which is equal to $P/3$. The other parameters have been described in Section 3.1. Equations (11)–(13) represent the distribution of heat sources when three LDs pump the crystal at $y \approx 12$ mm, $x \approx 0$ mm and $x \approx 12$ mm, respectively.

The boundary conditions for establishing the model of the Nd,Gd:SrF_2 crystal include two aspects, the ambient temperature T_0 and the air convection mechanism as follows:

$$\begin{cases} k_x \frac{\partial T}{\partial x} = h_{\mathrm{a}}(T - T_0) \\ k_y \frac{\partial T}{\partial y} = h_{\mathrm{a}}(T - T_0) \\ k_z \frac{\partial T}{\partial z} = h_{\mathrm{a}}(T - T_0) \end{cases}. \tag{14}$$

Nd,Gd:SrF_2 is an isotropic material with uniform thermal conductivity of k in all directions ($k_x = k_y = k_z = k$). Since the amplifier has no cooling device, it is assumed that all sides of the crystal are in contact with air, and the heat transfer coefficient is h_{a}. The values of the parameters in the thermal simulation are presented in Table 4.

5.2. Calculation results of temperature distribution

Figure 7 depicts the temperature distribution of Nd,Gd:SrF_2 over time. The output time step in Figures 7(a)–7(c) is set to 50 μs with a total simulation time of 5 s. Due to the hardware limitations, an 'adaptive timestepping scheme' is employed in COMSOL Multiphysics software to optimize memory usage and computational time. This scheme allows the software to automatically adjust the time step to maintain the tolerance, which is governed by physics[43]. In the y–z plane ($x = 0$ mm, Figure 7(a)) and x–y plane ($z = 3$ mm, Figure 7(b)), the highest temperatures are concentrated in the area where the Nd,Gd:SrF_2 crystal is pumped. As time progresses, the temperature in the pumped area gradually decreases, while the temperature in the surrounding area increases slightly due to heat conduction.

The temperature curves for the coordinate points (–0.055, 6, 3), (6, 6, 3) and (0, 0, 0) are shown in Figures 7(c) and 7(d) with all coordinates provided in millimeters. Figure 7(c) focuses on the temperature change within 5 s. At 0.005 s after the start of the pumping laser pulse, the highest temperature reached 293.254 K at (–0.055, 6, 3), and then decreased. A similar temperature trend is observed at (6, 6, 3). At (0, 0, 0), the temperature slowly increases from the ambient temperature. After 3 s from the start of the pumping laser pulse, the temperature at all three coordinate points stabilizes. To more accurately capture the highest temperatures at the three coordinate points, the output time step in Figure 7(d) is set to 10 μs with a simulation time of 0.03 s. The highest temperature is 296.109 K at (–0.055, 6, 3). Further reduction in the time step shows that the highest temperature remains virtually unchanged.

It can be postulated that the implementation of cooling devices, such as water cooling and heat sinks, may facilitate the operation of the laser at a repetition rate exceeding 1 Hz. Figure 8 shows a schematic diagram of a water cooling structure that can be referenced. Two cooling plates are in contact with the bottom and top surfaces of the crystal, respectively. Inside the cooling plates are many microfluidic channels, and the blue arrows indicate the direction of coolant flow. The heat deposited in the crystal can be dissipated by setting appropriate cooling temperatures and flow velocities[44]. The output performance of the laser remains almost unaffected as long as the temperature remains within tolerable limits over a period of 1 h.

5.3. Calculation model of stress distribution

The heat load creates a thermal gradient that can lead directly to stress in the crystal, and stress can cause adverse effects such as birefringence and thermal lensing. The stress

Table 4. Values of the parameters in the thermal simulation.

Parameter	ρ	C_{p}	t_{p}	k	P	S_{LD}	h_{a}	T_0
Value	4.46 g/cm^3	543 J/(kg·K)	500 μs	4 W/(m·K)	7200 W	20 mm^2	5 W/(K·m^2)	293.15 K

https://doi.org/10.1017/hpl.2025.26 Published online by Cambridge University Press

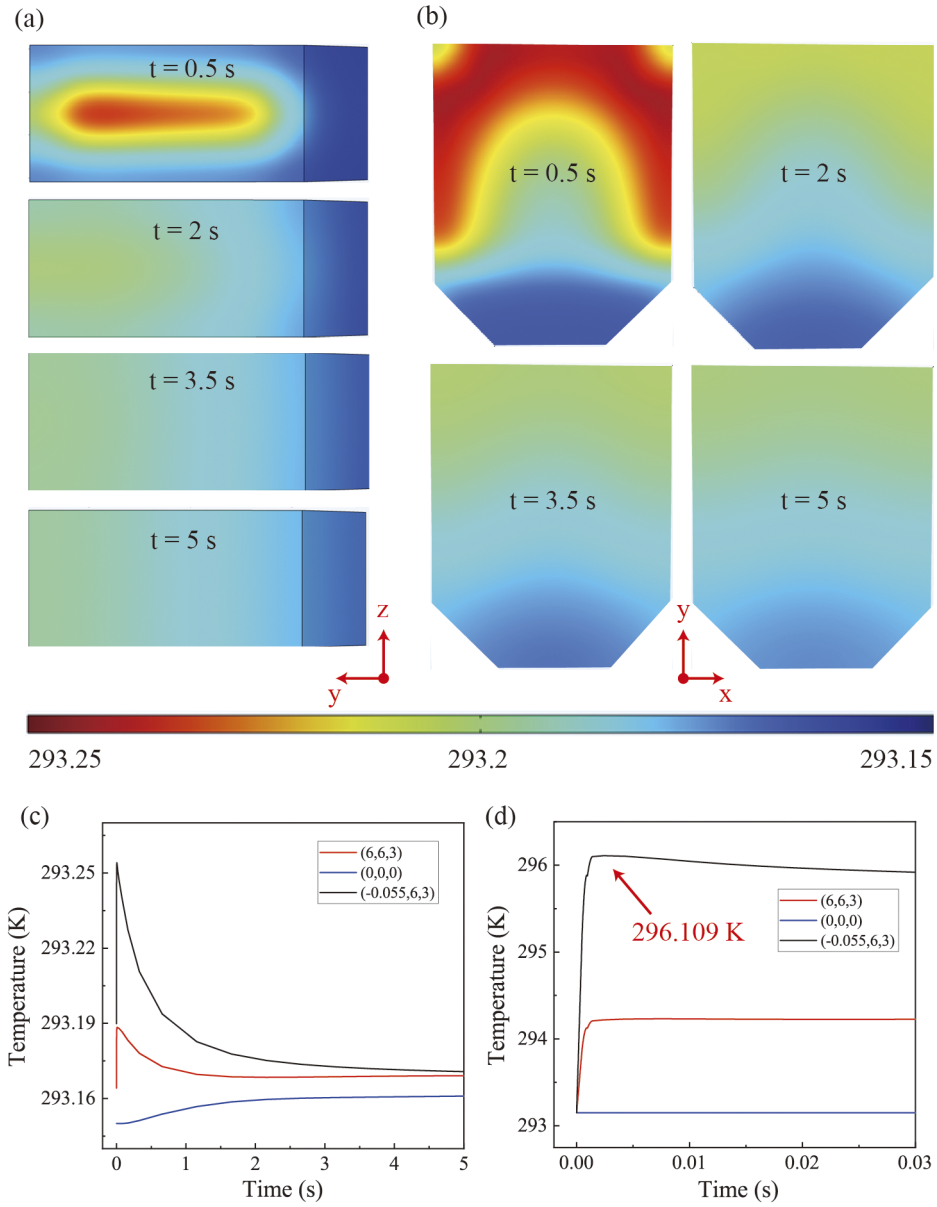

Figure 7. Temperature distribution of Nd,Gd:SrF_2 crystal. The perspectives are as follows: (a) y–z plane, $x = 0$ mm; (b) x–y plane, $z = 3$ mm; (c), (d) temperature distribution at three coordinate points.

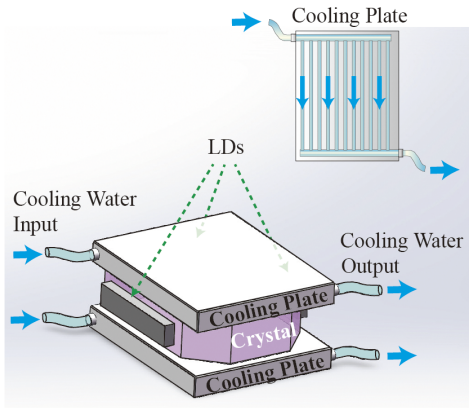

Figure 8. Schematic diagram of water cooling.

distribution of SrF_2 is also simulated using COMSOL Multiphysics software. In three dimensions, the stress (σ_s) and strain (ε_s) can be written as follows[45]:

$$\sigma_s = \begin{bmatrix} \sigma_{xx} & \sigma_{xy} & \sigma_{xz} \\ \sigma_{yx} & \sigma_{yy} & \sigma_{yz} \\ \sigma_{zx} & \sigma_{zy} & \sigma_{zz} \end{bmatrix}, \tag{15}$$

$$\varepsilon_s = \begin{bmatrix} \varepsilon_{xx} & \varepsilon_{xy} & \varepsilon_{xz} \\ \varepsilon_{yx} & \varepsilon_{yy} & \varepsilon_{yz} \\ \varepsilon_{zx} & \varepsilon_{zy} & \varepsilon_{zz} \end{bmatrix}, \tag{16}$$

where each element in ε_s is defined as a derivative of the displacements:

https://doi.org/10.1017/hpl.2025.26 Published online by Cambridge University Press

$$\begin{bmatrix} \varepsilon_{xx} \\ \varepsilon_{yy} \\ \varepsilon_{zz} \\ \varepsilon_{xy} \\ \varepsilon_{yz} \\ \varepsilon_{xz} \end{bmatrix} = \begin{bmatrix} \frac{\partial u}{\partial x} \\ \frac{\partial v}{\partial y} \\ \frac{\partial w}{\partial z} \\ \frac{1}{2}\left(\frac{\partial u}{\partial y} + \frac{\partial v}{\partial x}\right) \\ \frac{1}{2}\left(\frac{\partial v}{\partial z} + \frac{\partial w}{\partial y}\right) \\ \frac{1}{2}\left(\frac{\partial u}{\partial z} + \frac{\partial w}{\partial x}\right) \end{bmatrix}, \tag{17}$$

where u, v and w are the displacement vectors. The thermal strain ($\Delta\varepsilon_s$) is given by the following[46]:

$$\Delta\varepsilon_s = \alpha_e \Delta T, \tag{18}$$

where α_e is the thermal expansion coefficient, which is 18.4×10^{-6} K^{-1} for SrF_2, and ΔT is the temperature difference. The three dimensions generalization of Hooke's law can be written as follows:

$$\begin{bmatrix} \sigma_{xx} \\ \sigma_{yy} \\ \sigma_{zz} \\ \sigma_{xy} \\ \sigma_{yz} \\ \sigma_{xz} \end{bmatrix} = D \begin{bmatrix} \varepsilon_{xx} \\ \varepsilon_{yy} \\ \varepsilon_{zz} \\ \varepsilon_{xy} \\ \varepsilon_{yz} \\ \varepsilon_{xz} \end{bmatrix}. \tag{19}$$

For the isotropic SrF_2 crystal, D is a function of Young's modulus ($E_Y = 99.91 \times 10^9$ Pa) and Poisson's ratio ($\nu_P = 0.25$):

$$D = \frac{E_Y}{(1+\nu_P)(1-2\nu_P)} \begin{bmatrix} 1-\nu_P & \nu_P & \nu_P & 0 & 0 & 0 \\ \nu_P & 1-\nu_P & \nu_P & 0 & 0 & 0 \\ \nu_P & \nu_P & 1-\nu_P & 0 & 0 & 0 \\ 0 & 0 & 0 & \frac{1-2\nu_P}{2} & 0 & 0 \\ 0 & 0 & 0 & 0 & \frac{1-2\nu_P}{2} & 0 \\ 0 & 0 & 0 & 0 & 0 & \frac{1-2\nu_P}{2} \end{bmatrix}. \tag{20}$$

Since the bottom and top surfaces of the SrF_2 are expected to be clamped, their displacement changes are constrained to be zero. The values of the parameters related to temperature simulation are shown in Table 4.

5.4. Calculation results of stress distribution

The seed pulse is injected into the crystals at the end of the pump time, so the simulation time of stress distribution is set to 500 μs. The output time step is set to 50 μs. To verify the effectiveness of this time step, we simulate the temperature

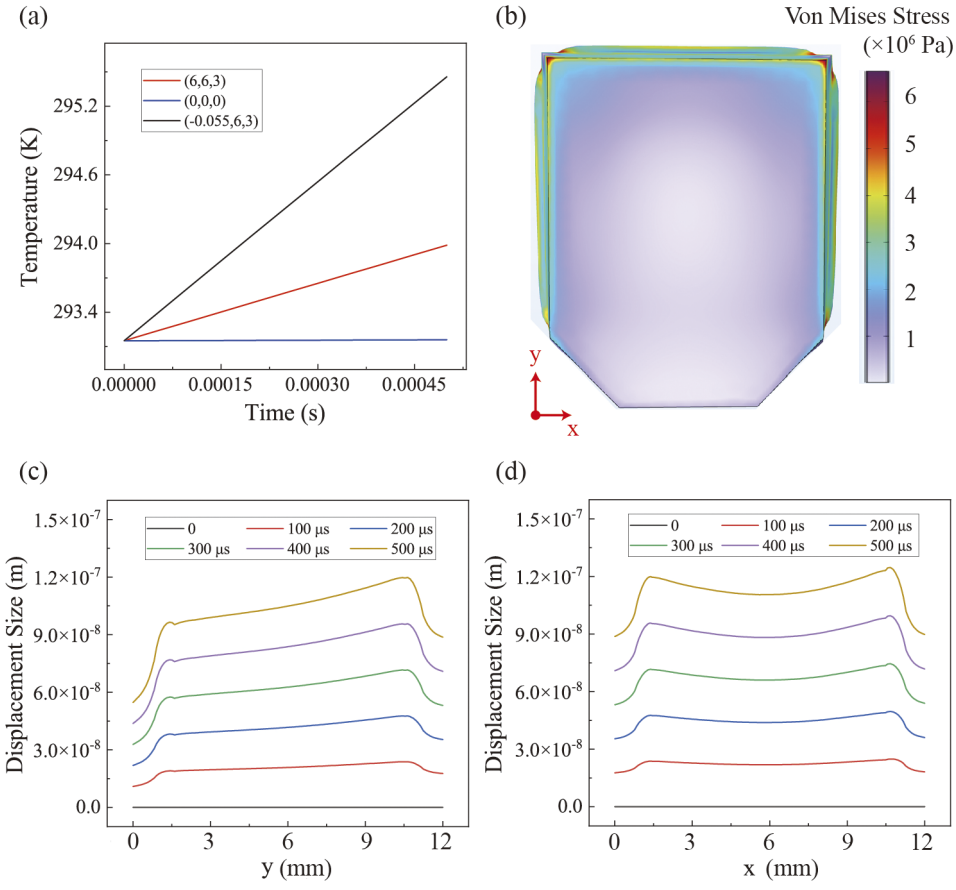

Figure 9. (a) Temperature as a function of time for three coordinate points. (b) Von Mises stress distribution in the x–y plane. (c) Displacement at different positions along the line segment from coordinate point (0, 0, 3) to (0, 12, 3). (d) Displacement at different positions along the line segment from coordinate point (0, 12, 3) to (12, 12, 3).

https://doi.org/10.1017/hpl.2025.26 Published online by Cambridge University Press

changes over time at three coordinate points, (–0.055, 6, 3), (6, 6, 3) and (0, 0, 0), as shown in Figure 9(a). The highest temperature of 295.458 K is obtained at (–0.055, 6, 3), which is consistent with the result at the same moment in Figure 7(d). The top view of the stress distribution in the x–y plane is shown in Figure 9(b), and the maximum stress is 6.6×10^6 Pa. To make the stress-induced deformation of the crystal more visible, the value is magnified by a factor of 6000 in Figure 9(b). It can be observed that the deformation occurs mainly in the three pumped areas, and the degree of deformation on the left- and right-hand sides is essentially the same.

Figure 9(c) shows the displacement at different positions along the line segment from coordinate point (0, 0, 3) to (0, 12, 3). The displacement size increases with the pump time, and the maximum displacement size is 1.198×10^{-7} m at 500 μs at coordinate point (0, 10.6, 3). Figure 9(d) shows the displacement at different positions along the line segment from coordinate point (0, 12, 3) to (12, 12, 3). There are two peaks near the positions $x = 1.3$ mm and $x = 10.7$ mm at different times. The maximum displacement size is 1.246×10^{-7} m at 500 μs at coordinate point (10.7, 12, 3). This work focuses on the simulation of the transient state with the backward differentiation formula[47]. In future steady-state analyses, the effects of thermally induced birefringence and thermal lensing can be explored in more detail.

6. Conclusion

A compact laser amplifier with high gain has been designed by utilizing two SrF_2 crystals. The gain length of the laser beam is extended due to TIR, and parasitic oscillations are suppressed by employing an irregular crystal geometry. When the pump time was set to 320 μs and the pump power increased from 3.6 to 7.2 kW, the presence of ASE resulted in a reduction of g_0 from 0.0764 to 0.1602 cm^{-1}. 0.5%Nd,5%Gd:SrF_2 and 0.5%Nd,5%Y:SrF_2 are used simultaneously to suppress the gain narrowing effect, leading to an output bandwidth more than twice that achieved with two identical crystals. To the best of our knowledge, this is the first proposal for a compact laser amplifier with a gain exceeding 10^6 based on different SrF_2 crystals. The compact amplifier has the potential for application in high-peak-power, high-energy laser devices, and the thermal properties of the crystals also make it possible to increase the operating repetition rate.

Acknowledgements

This work was supported by the National Major Project of China (Grant No. GFZX020503.10); the National Natural Science Foundation of China (Grant Nos. 12074353, 62405298 and 61925508); and the CAS Project for Young Scientists in Basic Research (Grant No. YSBR-024).

References

1. J. Zuo and X. Lin, Laser Photonics Rev. **16**, 2100741 (2022).
2. M. L. Spaeth, K. R. Manes, D. H. Kalantar, P. E. Miller, J. E. Heebner, E. S. Bliss, D. R. Speck, T. G. Parham, P. K. Whitman, P. J. Wegner, P. A. Baisden, J. A. Menapace, M. W. Bowers, S. J. Cohen, T. I. Suratwala, J. M. Di Nicola, M. A. Newton, J. J. Adams, J. B. Trenholme, R. G. Finucane, R. E. Bonanno, D. C. Rardin, P. A. Arnold, S. N. Dixit, G. V. Erbert, A. C. Erlandson, J. E. Fair, E. Feigenbaum, W. H. Gourdin, R. A. Hawley, J. Honig, R. K. House, K. S. Jancaitis, K. N. LaFortune, D. W. Larson, B. J. Le Galloudec, J. D. Lindl, B. J. Macgowan, C. D. Marshall, K. P. McCandless, R. W. Mccracken, R. C. Montesanti, E. I. Moses, M. C. Nostrand, J. A. Pryatel, V. S. Roberts,S. B. Rodriguez, A. W. Rowe, R. A. Sacks, J. T. Salmon, M. J. Shaw, S. Sommer, C. J. Stolz, G. L. Tietbohl, C. C. Widmayer, and R. Zacharias, Fusion Sci. Technol. **69**, 25 (2016).
3. C. Danson, D. Hillier, N. Hopps, and D. Neely, High Power Laser Sci. Eng. **3**, e3 (2015).
4. R. P. Drake, Nucl. Fusion. **59**, 035001 (2019).
5. D. Kraus, J. Vorberger, A. Pak, N. J. Hartley, L. B. Fletcher, S. Frydrych, E. Galtier, E. J. Gamboa, D. O. Gericke, S. H. Glenzer, E. Granados, M. J. MacDonald, A. J. MacKinnon, E. E. McBride, I. Nam, P. Neumayer, M. Roth, A. M. Saunders, A. K. Schuster, P. Sun, T. van Driel, T. Döppner, and R. W. Falcone, Nat. Astron. **1**, 606 (2017).
6. A. Li, C. Qin, H. Zhang, S. Li, L. Fan, Q. Wang, T. Xu, N. Wang, L. Yu, Y. Xu, Y. Liu, C. Wang, X. Wang, Z. Zhang, X. Liu, P. Bai, Z. Gan, X. Zhang, X. Wang, C. Fan, Y. Sun, Y. Tang, B. Yao, X. Liang, Y. Leng, B. Shen, L. Ji, R. Li, and Z. Xu, High Power Laser Sci. Eng. **10**, e26 (2022).
7. Y. Tzuk, C. Goren, and A. Tal, Appl. Opt. **48**, 1819 (2009).
8. J. Guo, J. Wang, X. Wang, X. Wang, W. Fan, and X. Li, Opt. Commun. **509**, 127874 (2022).
9. M. Zeyen, L. Affolter, M. A. Ahmed, T. Graf, O. Kara, K. Kirch, M. Marszalek, F. Nez, A. Ouf, R. Pohl, I. Schulthess, S. Rajamohanan, P. Yzombard, K. Schuhmann, and A. Antognini, Opt. Express **32**, 1218 (2024).
10. K. Yao, X. Xie, J. Tang, C. Fan, S. Gao, Z. Lu, X. Fu, X. Tian, K. Zheng, M. Fan, and Q. Zhu, Laser Phys. **29**, 115002 (2019).
11. Z. Qin, G. Xie, J. Ma, W. Ge, P. Yuan, L. Qian, L. Su, D. Jiang, F. Ma, Q. Zhang, Y. Cao, and J. Xu, Opt. Lett. **39**, 1737 (2014).
12. X. Zeng, K. Zhou, Y. Zuo, Q. Zhu, J. Su, X. Wang, X. Wang, X. Huang, X. Jiang, D. Jiang, Y. Guo, N. Xie, S. Zhou, Z. Wu, J. Mu, H. Peng, and F. Jing, Opt. Lett. **42**, 2014 (2017).
13. L. Pan, S. Ji, W. Huang, J. Guo, X. Lu, J. Wang, W. Fan, X. Li, and J. Zhu, Photonics **8**, 96 (2021).
14. X. Li, Q. Hao, D. Jiang, Q. Wu, Z. Zhang, Z. Zhang, J. Liu, and L. Su, Opt. Mater. Express **10**, 704 (2020).
15. S. A. Payne, J. A. Caird, L. L. Chase, L. K. Smith, N. D. Nielsen, and W. F. Krupke, J. Opt. Soc. Am. B **8**, 726 (1991).
16. Z. Zhou, Y. Zhang, X. Liu, B. Mei, L. Zhou, J. Qin, and D. Yuan, J. Alloys Compd. **926**, 166898 (2022).
17. F. Ma, H. Zhou, Q. Tang, L. Su, M. Zhang, P. Zhang, H. Yin, Z. Li, Q. Lv, and Z. Chen, J. Alloys Compd. **899**, 162913 (2022).
18. F. Zhang, X. Fan, J. Liu, F. Ma, D. Jiang, S. Pang, L. Su, and J. Xu, Opt. Mater. Express **6**, 1513 (2016).
19. F. Ma, D. Jiang, L. Su, Z. Zhang, X. Tian, F. Zhang, and J. Liu, J. Lumin. **219**, 116911 (2020).
20. V. Kubeček, M. Jelínek, M. Čech, D. Vyhlídal, F. Ma, D. Jiang, and L. Su, in *2018 Conference on Lasers and Electro-Optics Pacific Rim* (2018), paper F2E.4.
21. F. Zhang, J. Liu, W. Li, B. Mei, D. Jiang, X. Qian, and L. Su, Opt. Eng. **55**, 106114 (2016).
22. J. Zhu, L. Wei, W. Tian, J. Liu, Z. Wang, L. Su, J. Xu, and Z. Wei, Laser Phys. Lett. **13**, 055804 (2016).

https://doi.org/10.1017/hpl.2025.26 Published online by Cambridge University Press

23. L. Wei, H. Han, W. Tian, J. Liu, Z. Wang, Z. Zhu, Y. Jia, L. Su, J. Xu, and Z. Wei, Appl. Phys. Express **7**, 092704 (2014).
24. J. Chen, Y. Peng, Z. Zhang, H. Su, Y. Leng, D. Jiang, F. Ma, X. Qian, F. Tang, and L. Su, Opt. Commun. **382**, 201 (2017).
25. J. Guo, J. Wang, X. Lu, Y. Zhang, X. Wang, Z. Zhang, D. Jiang, L. Su, W. Fan, and X. Li, Opt. Commun. **557**, 130298 (2024).
26. Z. Lu, Z. Zhang, D. Jiang, H. Kou, B. Zhang, Z. Xu, Y. Zhao, A. Wu, and L. Su, CrystEngComm **31**, 4130 (2024).
27. E. W. Gaul, M. Martinez, J. Blakeney, A. Jochmann, M. Ringuette, D. Hammond, T. Borger, R. Escamilla, S. Douglas, W. Henderson, G. Dyer, A. Erlandson, R. Cross, J. Caird, C. Ebbers, and T. Ditmire, Appl. Opt. **49**, 1676 (2010).
28. C. V. Filip, Opt. Express **19**, 20953 (2011).
29. H. Cao, X. Lu, and D. Fan, Appl. Opt. **51**, 2150 (2012).
30. H. H. Li, J. Phys. Chem. Ref. Data **9**, 161 (1980).
31. X. Chen and J. Xu, Acta Opt. Sin. **27**, 1827 (2007).
32. I. Snetkov, A. Yakovlev, and O. Palashov, Opt. Mater. **69**, 291 (2017).
33. X. Wang, X. Li, J. Wang, J. Guo, X. Lu, Q. Xiao, and W. Fan, J. Opt. Soc. Am. B **38**, 2707 (2021).
34. W. Koechner, *Solid-state Laser Engineering*, 6th ed., Springer Series in Optical Sciences (Springer Science+Business Media, Inc., 2006), p. 112.
35. L. Guo, S. Gao, D. Wu, W. Lv, Y. Li, and A. Li, High Power Laser Particle Beams **23**, 577 (2011).
36. L. Xiong, L. Cai, Y. Zheng, H. Liu, P. Zhang, Z. Nie, and X. Liu, Opt. Laser Technol. **77**, 1 (2016).
37. X. Liu, W. Zhao, L. Xiong, and H. Liu, *Packaging of High Power Semiconductor Lasers*, Springer Series in Micro- and Opto-electronic Materials, Structures, and Systems (Springer Science+Business Media, Inc., 2015), pp. 106–152.
38. Y.-H. Chuang, L. Zheng, and D. D. Meyerhofer, IEEE J. Quantum Electron. **29**, 270 (1993).
39. R. Adair, L. L. Chase, and S. A. Payne, Phys. Rev. B **39**, 3337 (1989).
40. F. Ma, Z. Zhang, D. Jiang, Z. Zhang, H. Kou, A. Strzep, Q. Tang, H. Zhou, M. Zhang, P. Zhang, S. Zhu, H. Yin, Q. Lv, Z. Li, Z. Chen, and L. Su, Cryst. Growth Des. **22**, 4480 (2022).
41. M. D. Perry, T. Ditmire, and B. C. Stuart, Opt. Lett. **19**, 2149 (1994).
42. M. B. Bavil and E. Safari, J. Mech. Sci. Technol. **28**, 3231 (2014).
43. https://www.comsol.com/support/knowledgebase/1254.
44. R. S. Nagymihaly, H. Cao, D. Papp, G. Hajas, M. Kalashnikov, K. Osvay, and V. Chvykov, Opt. Express **25**, 6664 (2017).
45. https://www.comsol.com/multiphysics/introduction-to-structural-mechanics.
46. D. V. N. Harish, A. Bharatish, H. N. Narasimha Murthy, B. Anand, and K. N. Subramanya, Ceram. Int. **47**, 3498 (2021).
47. https://www.comsol.com/support/knowledgebase/1062.

https://doi.org/10.1017/hpl.2025.26 Published online by Cambridge University Press